HHS Public Access

Author manuscript

Neuron. Author manuscript; available in PMC 2020 November 06.

Published in final edited form as:

Neuron. 2019 November 06; 104(3): 451–457.e3. doi:10.1016/j.neuron.2019.08.004.

Functional logic of layer 2/3 inhibitory connectivity in ferret visual cortex

Benjamin Scholl[1], **Daniel E. Wilson**[2], **Juliane Jaepel**[1], **David Fitzpatrick**[1]

[1]Max Planck Florida Institute for Neuroscience, 1 Max Planck Way, Jupiter, FL, 33458

[2]Harvard Medical School, Boston, MA 02115 USA

Summary

Understanding how cortical inhibition shapes circuit function requires identifying the connectivity rules relating the response properties of inhibitory interneurons and their postsynaptic targets. Here we explore the orientation tuning of layer 2/3 inhibitory inputs in ferret visual cortex using a combination of *in vivo* axon imaging, functional input mapping, and physiology. Inhibitory boutons exhibit robust orientation tuned responses with preferences that can differ significantly from the cortical column in which they reside. Inhibitory input fields measured with patterned optogenetic stimulation and intracellular recordings revealed that these inputs originate from a wide-range of orientation domains, inconsistent with a model of co-tuned inhibition and excitation. Intracellular synaptic conductance measurements confirm that neurons could depart from a co-tuned regime. Our results argue against a simple rule for the arrangement of inhibitory inputs supplied by layer 2/3 circuits and suggest that heterogeneity in presynaptic inhibitory networks contribute to neural response properties.

eTOC Blurb

Scholl et al. examine the functional connectivity of layer 2/3 inhibitory inputs onto single neurons in ferret visual cortex. This study argues against a simple rule describing the arrangement of inhibitory inputs supplied by layer 2/3 circuits.

Introduction

Cortical circuits are endowed with inhibitory interneurons that can influence the activity and sensory responses of neighboring cells (Heeger, 1999; Isaacson and Scanziani, 2011). Elucidating the exact function of cortical inhibitory neurons requires a complete

Corresponding author: Benjamin Scholl, scholl.ben@gmail.com.

Author contributions

B.S., D.E.W., and D.F. conceived experiments. B.S., D.E.W., and J.J. performed experiments. B.S. analyzed data. B.S., J.J., and D.F. wrote the paper.

Lead Contact: Benjamin Scholl, scholl.ben@gmail.com

Competing financial interests

The authors declare no competing financial interests.

understanding of their functional connectivity: the response properties of inhibitory interneurons and their postsynaptic excitatory targets. While recent studies have begun unraveling the functional properties of excitatory inputs onto postsynaptic excitatory targets (Chen et al., 2013; Iacaruso et al., 2017; Lee et al., 2016; Scholl et al., 2017; Wertz et al., 2015; Wilson et al., 2016), the response properties and arrangements of inhibitory inputs onto individual postsynaptic targets remain poorly understood.

The net synaptic drive of inhibitory and excitatory inputs to individual pyramidal neurons in the cortex is generally considered to be co-tuned, such that the orientation tuning of inhibition matches the orientation tuning of excitation as assayed by *in vivo* intracellular recordings of synaptic conductances (Adesnik, 2017; Anderson et al., 2000; Liu et al., 2011; Priebe and Ferster, 2005; Tan et al., 2011; Wehr and Zador, 2003; Wu et al., 2008). These measurements, however, provide only a gross estimate of the total synaptic input summed at the soma, obscuring contributions from individual interneurons or particular cortical layers, and within this average there may be departures from a co-tuning framework. Slice physiology experiments examining connections between individual inhibitory interneurons and surrounding excitatory pyramidal cells have revealed subtype-specific and distance-dependent wiring rules (Fino and Yuste, 2011; Kätzel et al., 2010; Oswald et al., 2009; Watkins et al., 2014; Yoshimura and Callaway, 2005). For instance, it is thought that parvalbumin basket cells non-specifically inhibit surrounding pyramidal cells in a spatially-dependent manner (Hofer et al., 2011; Levy and Reyes, 2012; Packer and Yuste, 2011). In rodent primary visual cortex (V1), this dense connectivity is thought to potentially act as a gain control mechanism (Fino and Yuste, 2011; Isaacson and Scanziani, 2011) as parvalbumin expressing cells are generally broadly tuned for visual stimuli (Hofer et al., 2011; Scholl et al., 2015). Thus, departures from a co-tuning framework could arise with inhibitory inputs originating from cells unselective to sensory features, inhibitory inputs from a diversity of selective cells, or a combination of these arrangements.

In ferret and cat V1, layer 2/3 inhibitory cells are selective for orientation and direction, indistinguishable from neighboring excitatory neurons (Hirsch et al., 2003; Wilson et al., 2017). Given the selectivity and organization of inhibitory neurons in these circuits, it is unclear what the logic of their connectivity is and whether it is consistent with a co-tuning framework. Layer 2/3 inhibitory inputs might exhibit co-tuning with that of postsynaptic targets (Anderson et al., 2000; Tan et al., 2011; Wehr and Zador, 2003), which could originate from inhibitory interneurons in the same cortical column or through long-range projections from co-tuned cortical domains (Gilbert and Wiesel, 1989; Bosking et al., 1997). It is also possible that the columnar arrangement of inhibitory axonal projections exhibits less specificity, yielding weaker tuning (Liu et al., 2011; Wu et al., 2008), a lack of tuning altogether, or differential tuning relative to the preferences of postsynaptic targets (Wilson et al., 2018).

To probe the functional organization of layer 2/3 inhibition in ferret V1, we first performed *in vivo* calcium imaging of layer 2/3 GABAergic boutons. We measured functional properties of these projections with respect to the orientation map, finding a surprising degree of mismatch between bouton orientation preference and the local orientation domain. We then used *in vivo* intracellular optogenetic connectivity mapping to identify the

arrangement of layer 2/3 inhibitory inputs onto individual excitatory neurons. We compared orientation tuning of subthreshold membrane potential of excitatory neurons with cortical inhibitory input fields, leveraging the columnar organization of orientation preferences for excitatory and inhibitory cells. While inhibitory input fields could exhibit distinct characteristics, overall they were not cotuned with subthreshold tuning of postsynaptic targets. Instead, layer 2/3 inhibitory inputs originated from a wide range of orientation domains, providing functionally broad inhibition across the population of cells we recorded. Finally, to determine how this connectivity might contribute to the orientation tuning of inhibition and excitation of individual layer 2/3 neurons, we measured synaptic conductance demonstrating that the inhibitory orientation tuning exhibits considerable cell to cell variation, including examples where inhibition and excitation depart from a co-tuned regime. Our data suggest that inputs supplied by layer 2/3 inhibitory neurons have a functionally broad impact on postsynaptic targets, which could allow for diversity in how cortical inhibition impacts circuit function.

Results

To explore the role of layer 2/3 inhibitory inputs, we first evaluated the functional specificity of GABAergic axons relative to the columnar map of orientation preference. Axonal projections of inhibitory interneurons in carnivores can span distances beyond a few hundred microns (Roerig and B. Chen, 2002). In ferret V1, orientation preferences of both excitatory and inhibitory neurons exhibit a columnar organization, which corresponds to the intrinsic map of orientation preference (Wilson et al., 2018). Using adenoassociated virus to express GCaMP6s under the mDlx enhancer, we performed *in vivo* two-photon calcium imaging of inhibitory axonal boutons to characterize their orientation tuning (Fig. 1). We then measured the orientation preference map with intrinsic signal imaging of the local cortical regionfor comparison with the spatial distribution of individual bouton orientation preferences (Fig. 1b).

Some individual inhibitory axonal boutons were highly selective for orientation and prefered distinct orientations compared to the intrinsic orientation map at the same cortical location (Fig. 1a–d). Across our population of visually-driven boutons (see Methods; n = 8 fields of view), a substantial fraction was orientation-selective (OSI > 0.15: 85.4%), but individual boutons displayed a wide range of selectivities (OSI range = 0.99, 0.33 ± 0.26, median ± IQR; Fig. 1f). Focusing on boutons with responses well-fitted by a Gaussian tuning curve (r^2 > 0.5) and orientation selective (OSI > 0.15), we compared the orientation preference of individual bouton (n = 540) with the local intrinsic signal orientation preference (see Methods). Overall, boutons were tuned differentially to local cortical regions ($\Delta\Theta$ = 44.0 deg ± 30.0, circular mean ± s.d.; Fig. 1g). Of the individual fields of view we imaged, less than half (n = 3/8) displayed co-tuning with the local cortical region that was significantly greater than chance (Monte Carlo Significance Test).

Intrinsic signal imaging provides a coarse measure of orientation preference, so it is possible that greater layer 2/3 inhibitory specificity emerges with finer-scale measurements. To more accurately compare GABAergic boutons and their locality, we expressed GCaMP6s in GABAergic cells and jRGECO1a in excitatory cells (see Methods). Within each cortical

region, we compared the orientation preference of individual GABAergic boutons to local two-photon pixel-based orientation maps of excitatory cell activity (radius = 12.5 μm, see Methods) (Fig. 1i–j). We again found a lack of co-tuning between GABAergic boutons and the local orientation map ($\Delta\Theta$ = 47.3 deg ± 22.6, circular mean ± s.d.; n = 141 boutons; Fig. 1m). Using these data, we also examined bouton co-tuning with respect to distance from injection sites and found no significant correlation (r = 0.016, p = 0.98, circular-linear correlation). Together, these datasets reveal that a substantial fraction of GABAergic boutons reside in domains that are distinct from their orientation preference, and suggest that layer 2/3 inhibitory neurons may synapse onto postsynaptic targets that differ substantially from their orientation preference.

To better understand the functional identity of inhibitory inputs converging onto individual layer 2/3 neurons, we employed *in vivo* mapping of functional connectivity (Fig. 2). We expressed Channelrhodopsin restricted to the soma and proximal dendrites of layer 2/3 GABAergic interneurons using the mDlx enhancer (Dimidschstein et al., 2016) and a Kv2.1 targeting motif (see Methods) to prevent stimulation of fibers of passage and enhance the effective resolution (Baker et al., 2016; Wu et al., 2013). We then used whole-cell patch-clamp recordings to measure subthreshold membrane potential (V_m) of putative excitatory neurons in V1 to drifting gratings (Fig. 2a) and patterned photostimulation to activate inhibitory cells in small cortical regions (100-200 μm, see Methods, Fig. 2b) (Dhawale et al., 2010). Optogenetic stimulation of single cortical locations evoked robust inhibitory postsynaptic potentials (IPSPs) (Fig. 2c). To compare the functional origins of IPSPs relative to postsynaptic cells, we leveraged the columnar organization of inhibitory neuron orientation preferences (Wilson et al., 2018) (Fig. 2d). We compared V_m orientation tuning with the average inhibitory weight originating from different orientation domains (Fig. 2e–g). We calculated inhibitory weights by first normalizing IPSP amplitudes within each recording to the largest IPSP evoked, and then examining normalized IPSP amplitudes relative to cortical orientation domains (see Methods).

Inhibitory input fields onto postsynaptic targets were diverse. Some cells received inhibitory input from matching orientation domains, exhibiting co-tuning (Fig. 2f), while others appeared connected to inhibitory cells residing in differentially-tuned orientation domains (Fig. 2 e & g). Strict co-tuning between inhibitory input field and V_m was atypical; rather, inhibitory input generally originated from a range of orientation preferences (Fig. S1). The various functional arrangements of inhibitory inputs we observed led us to wonder whether there was any relationship with the diversity of V_m orientation tuning in postsynaptic cells. To characterize postsynaptic cell tuning, we computed an orientation selectivity index for V_m responses (OSI_{Vm}, see Methods). Across our population (n = 15), OSI_{Vm} was not correlated with the amount of inhibitory input from co-tuned orientation domains (r = 0.11, p = 0.35) or differentially-tuned orientation domains (r = −0.03, p = 0.54).

While layer 2/3 inhibitory input fields onto individual cells were often distinct, many cells received functionally broad inhibitory input (Fig. 2e–f, Fig. S1). We then asked whether inhibitory input field breadth related to postsynaptic cell selectivity (OSI_{Vm}). Average inhibitory input fields were identical for cells with low (OSI_{Vm} < 0.15; n = 7) or high (OSI_{Vm} > 0.15; n = 8) selectivity (Fig. 3a). Both received similar amounts of inhibition from

co-tuned and differentially-tuned cortical domains (OSI_{Vm} < 0.15: p = 0.29; OSI_{Vm} > 0.15: p = 0.53). We also found equivalent fractions of inhibitory input originating from co-tuned and differentially--tuned cortical domains near the recording pipette (< 300 μm; OSI_{Vm} < 0.15: p = 0.94; OSI_{Vm} > 0.15: p = 0.73; Fig. 3 b–c) and for distal cortical locations (> 300 μm; OSI_{Vm} < 0.15: p = 0.14; OSI_{Vm} > 0.15: p = 0.68). Overall, these data show that individual excitatory neurons receive a broad palette of layer 2/3 inhibitory inputs irrespective of their selectivity.

Our measurements of layer 2/3 inhibitory connectivity show only a small fraction of inhibitory inputs originate from co-tuned orientation domains, contrasting with previous studies suggesting inhibition and excitation are generally co-tuned (Adesnik, 2017; Anderson et al., 2000; Liu et al., 2011; Priebe and Ferster, 2005; Tan et al., 2011; Wehr and Zador, 2003; Wu et al., 2008). This raises the question of whether layer 2/3 neurons in ferret visual cortex exhibit more broadly-tuned inhibition during visual stimulation that would be consistent with the results of the connectivity mapping experiments. To address this question, we performed whole-cell recordings with a Cs+-based internal solution while recording V_m responses to drifting gratings at different current steps to extract synaptic conductances and their orientation tuning (see Methods). In some cells, synaptic excitation (Ge) and inhibition (Gi) were co-tuned as previously described (Fig. 4a, left; see also Fig. S2). However, other cells were differentially tuned for Ge and Gi (Fig. 4a, right; see also Fig. S2). To quantify the nature of Ge and Gi tuning, we computed the ratio of inhibition relative to excitation (Gi/Ge) for responses near the preferred or non-preferred orientation of Ge (θ_{Ge} < 30° and θ_{Ge} > 30°, respectively). We found that half the cells in our population exhibited significantly greater Gi/Ge for non-preferred orientations compared to the preferred (n = 4/8, bootstrapped confidence intervals; Fig. 4b). In the remaining cells (n = 4/8), Gi/Ge for both sets of stimuli were not significantly different, consistent with co-tuning. These measurements of synaptic conductances reveal a diversity of inhibitory input profiles for individual layer 2/3 pyramidal neurons in ferret visual cortex including co-tuning, broad tuning, or differential tuning of inhibition relative to excitation.

Discussion

Here we found that in ferret V1, layer 2/3 GABAergic inputs onto pyramidal cells originate from cortical domains exhibiting a broad-range of orientation preferences. Inhibitory input fields were diverse, reflecting some layer 2/3 inhibitory specificity rather than a broad, nonspecific input onto individual cells. These data were supported by a wide-range of orientation preferences observed in GABAergic boutons occupying orientation domains. On average, however, excitatory cells received layer 2/3 inhibitory input originating from equivalent fractions of co-tuned and differentially-tuned cortical domains, irrespective of either postsynaptic cell orientation selectivity or cortical distance of connected inhibitory neurons. Finally, we found that co- and differentially-tuned inhibition is evident at the level of synaptic conductance, demonstrating that individual cells can receive co-tuned, broadly-tuned, or differentially-tuned inhibition relative to excitation.

Previous studies suggest that inhibition and excitation received by cortical neurons are generally co-tuned (Anderson et al., 2000; Liu et al., 2011; Priebe and Ferster, 2005; Tan et

al., 2011; Wehr and Zador, 2003; Wu et al., 2008), in contrast to multiple lines of evidence presented here. One obvious difference from previous studies in the visual cortex is that they focused on conductance measurements from thalamorecipient neurons in layer 4, while the experiments described here were focused on layer 2/3. Laminar differences in the rules governing the arrangement of excitatory and inhibitory synaptic inputs could explain differences in the response properties of neurons in these two layers (Martinez et al., 2005; Priebe et al., 2004). We also note that given the technical difficulty of sampling local inhibition from within an orientation column *in vivo,* we potentially underestimate the contribution of local co-tuned inputs.

It is worth emphasizing that there are many reasons why conductance and connectivity measures yield different pictures of the organization of excitatory and inhibitory inputs to individual neurons. Measurements of synaptic conductances *in vivo* reflect the activity of the entire circuit in response to visual stimulation, while connectivity measures are limited to the elements of the circuit being tested. Our connectivity mapping experiments focus specifically on inputs derived from layer 2/3 inhibitory neurons, only one of many possible sources of inhibition to layer 2/3 neurons. Conductance measurements of inhibitory and excitatory inputs could access additional sources of inhibitory input, such as those derived from interlaminar projections (Bortone et al., 2014). But even limiting our consideration to layer 2/3 inhibitory circuits, the tuning derived from connectivity patterns could be strikingly different from the tuning attributable to layer 2/3 inhibition during the presentation of visual stimuli. Different visual stimuli are likely to induce a pattern of activity in layer 2/3 inhibitory circuits that is not sampled in the connectivity mapping experiments, a bias that reflects how the full complexity of V1 circuits engage the connectivity matrix of layer 2/3 neurons.

In many ways, functional connectivity measurements are best viewed as the range of possible synaptic inputs that can be driven with sensory input. Specific subpopulations within the total possible inhibitory input population could be recruited in a manner dependent on the type and strength of incoming sensory inputs (Ben-Yishai et al., 1995; Douglas and Martin, 2007; Rubin et al., 2015). In this way, broad inhibitory input fields derived from populations of inhibitory neurons that are well-tuned to stimulus orientation may form the basis for a range of orientation-specific operations that can be induced by different patterns of visual stimulation. The presence of *both* co-tuned and differentially-tuned inputs onto an individual cell in ferret V1 could provide a means to supply different patterns of inhibition relative to the network activity or incoming sensory input. For example, in a single neuron, the presentation of oriented gratings could evoke inhibition co-tuned to excitation, while the direction of motion of the same drifting gratings could recruit differential-tuned inhibitory input (Wilson et al., 2018). Similarly, binocular visual stimulation is thought to drive distinct inhibitory networks compared to monocular stimulation in the same cells (Scholl et al., 2013; Zhao et al., 2013). Behavioral context is also shown to modulate inhibitory input onto individual cells through cholinergic innervation, suggesting that cholinergic inputs might activate inhibitory inputs not driven by passive sensory input (Kuchibhotla et al., 2017).

A full understanding of the functional complexity of inhibitory inputs requires delineating (1) the tuning properties of individual inputs, (2) the full range of inputs that converges on a neuron, and (3) how this inhibitory matrix is engaged under different stimulus conditions and/or cortical states. Our results suggest that the inhibitory inputs to individual layer 2/3 neurons in ferret visual cortex could support a large variety of distinct activation patterns, but identifying these functional motifs will require combining visual stimulation with population imaging to define the active population of inhibitory neurons, along with intracellular recording to define inhibitory input connectivity patterns and assess the impact of different stimulus induced inhibitory network activity patterns on pyramidal cell responses.

STAR Methods

LEAD CONTACT AND MATERIALS AVAILABILITY

Further information and request for resources and reagents should be directed to and will be fulfilled by the Lead Contact, Benjamin Scholl (scholl.ben@gmail.com).

EXPERIMENTAL MODEL AND SUBJECT DETAILS

All procedures were performed according to NIH guidelines and approved by the Institutional Animal Care and Use Committee at Max Planck Florida Institute for Neuroscience. Female ferrets (*Mustela putorius furo,* Marshall Farms) were used in all experiments. Animals underwent survival injections at ages P18-P23, followed by acute experiments preformed at ages P46-P58. Animals were housed in a vivarium under 12h light / 8h dark cycle. No *a priori* sample size estimation was preformed, but sample sizes are similar to other studies which preformed *in vivo* physiology.

METHOD DETAILS

Viral Injection—Ferrets aged P18-23 were anesthetized with isoflurane (delivered in O2). Atropine was administered and a 1:1 mixture of lidocaine and bupivacaine was administered SQ. Animals were maintained at an internal temperature of 37 degrees Celsius. Under sterile surgical conditions, a small craniotomy (0.8 mm diameter) was made over the visual cortex (7-8mm lateral and 2-3mm anterior to lambda). For imaging of GABAergic axons, we injected 5-30 nl of AAV1.mDlx.GCaMP6s at 400 and 200 mm below the pia. In some experiments, we co-injected AAV1/2-hSyn-jRGECO1a (~1uL). For STOMPM (see below), we injected ~1μl of AAV1-mDlx-ChR2-Flag-Kv2.1-p2a-H2b-CyRFP. Finally, the craniotomy was filled with sterile 1 % w/v agarose (Type IIIa, Sigma-Aldrich) and the incision site was sutured.

Cranial Window—After 3-5 weeks of expression, ferrets were anesthetized with 50mg/kg ketamine and isoflurane. Atropine and bupivacaine were administered, animals were placed on a feedback-controlled heating pad to maintain an internal temperature of 37 degrees Celsius, and intubated to be artificially respiratied. Isoflurane was delivered throughout the surgical procedure to maintain a surgical plane of anesthesia. An intravenous cannula was placed to deliver fluids. Tidal CO_2, external temperature, and internal temperature were continuously monitored. The scalp was retracted and a custom titanium headplate adhered to

the skull (Metabond, Parkell). A craniotomy was performed and the dura retracted to reveal the cortex. For axon imaging, 1-2 pieces of custom coverglass (3mm diameter, 0.7mm thickness, Warner Instruments) were adhered to a larger coverglass (8mm diameter, #1.5 thickness, Electron Microscopy Sciences) using optical adhesive (# 71, Norland Products) and placed onto the brain to gently compress the underlying cortex and dampen biological motion during imaging. A 1:1 mixture of tropicamide ophthalmic solution (Akorn) and phenylephrine hydrochloride ophthalmic solution (Akorn) was applied to both eyes to dilate the pupils and retract the nictating membranes. Contact lenses were inserted to protect the eyes. Upon completion of the surgical procedure, isoflurane was gradually reduced and pancuronium (2 mg/kg/hr) was delivered IV.

Two photon imaging—Two photon imaging was performed on a Bergamo II microscope (Thorlabs) running Scanimage (Pologruto et al., 2003) (Vidrio Technologies) with 940nm or 1050nm dispersion-compensated excitation provided by an Insight DS+ (Spectraphysics). For axon imaging, power after the objective was limited to a maximum of 60 mW, dependent on depth. Locations were selected for imaging on the basis of their position relative to large blood vessels, responsiveness to visual stimulation, and lack of prolonged calcium transients resulting from over-expression of GCaMP6s. Images were collected at 30 Hz using bidirectional scanning with 512×512 pixel resolution. Images were collected at 512×512 pixel resolution with fields of view 100 (GCaMP6s) or 200 (jRGECO1a) μm on a side.

Visual Stimuli—Visual stimuli were generated using Psychopy (Peirce, 2007). The monitor was typically placed 25 cm from the animal. For whole cell recordings, we optimized the preferred spatial frequency of the stimulus for the cell being recorded. Typical preferred spatial frequencies ranged from 0.04 to 0.25 cycles per degree.

Physiology—Recordings were performed by inserting a pipette through an agarose-filled craniotomy, or by using a coverglass with a hole drilled for pipette access. A silver-silver chloride reference electrode was inserted into the agarose or muscle. Recordings were made in current clamp mode. For measurements of membrane potential tuning and connectivity mapping, pipettes of 5-8 megaohm resistance were pulled using borosilicate glass (King Precision Glass) and filled with an intracellular solution containing (in mM) 135 K gluconate, 4 KCl, 10 HEPES, 10 Na2-phosphocreatine, 4 Mg-ATP, 0.3 Na3GTP, 0-0.1 Alexa 594 or 488, pH 7.2, 295 mOsm. Neurons were recorded from layer 2/3 (100 to 800 mm below the pia) using a Multiclamp 700B (Molecular Devices). Series resistance and pipette capacitance were corrected online. Series resistance for recordings typically ranged from 20-80 MW. Analog signals were digitized using Spike2 (CED). For measurements of synaptic conductances, the internal solution contained (in mM) 135 Cs-MeSO4, 10 QX-314, 4 TEA-Cl, 2 EGTA, 2 MgATP, 10 HEPES, 10 Na2-Phosphocreatine, pH 7.3, 295 mOsm and pipettes were typically 6-9 MW. Capacitance compensation was corrected online and series resistance was corrected online or offline. Conductance measurements typically began around 30 minutes after break-in to allow the internal solution of the pipette to dialyze the cell, eliminating action potentials and depolarizing the resting V_m as expected with the use of Cs+ and QX-314.

Somatic-targeted optogenetic membrane potential mapping (STOMPM) of connectivity—Connectivity mapping was performed on a custom-built microscope based off previously published designs (Dhawale et al., 2010). A DLP projector (X600, Optoma) with its color wheel removed was mounted to a tilt platform (Siskiyou) and linear stage (Thorlabs). A 50mm f/1.4 SLR lens (Nikkor) was mounted as close as possible to the projector and coupled to an achromatic doublet (AC508-150-A). Light passed through a blue dichroic filter (52-532, Edmund Optics) and was reflected onto the sample using a dichroic mirror (T495LPXR, Chroma), and focused onto the sample using a 35mm f/2.0 SLR lens (Nikkor). Emission light passed through a 105mm f2.0 lens (Nikkor) and an emission filter (FF01-600) and was imaged onto a camera (Xyla, Andor) controlled by Micromanager (http://www.micro-manager.org). Single pixels on the DMD corresponded to 4mm at the sample. Diffuse background light was 0.1 mW/mm2. Opsin was restricted to the soma using the Kv2.1 targeting motif (Baker et al., 2016; C. Wu et al., 2013). Before obtaining whole-cell recordings, we focused excitation light on the cortical surface. Then, we centered a stimulation grid on the pipette and delivered 25-50 trials of random grid stimulation. Spots were typically 100-200 μm FWHM, 1-3 mW power, and displayed for 100ms. We used positive current injection to depolarize the cell and increase the driving force for IPSPs. Previous measurements show that IPSP amplitude depends on pre-stimulus resting membrane potential, confirming that we are driving inhibitory inputs rather than causing reductions in spontaneous EPSPs (see Supplementary Figure 7 in Wilson et al., 2018). We likely underestimate input field sizes due to limitations in the spatial spread of virus injection, blue light absorption in blood vessels, and experimental geometry in which the large patch pipette interferes with light stimulation. We calculated inhibitory weights by first normalizing IPSP amplitudes within each record to the largest IPSP evoked and then examined normalized IPSP amplitudes relative to cortical orientation domains.

Intrinsic signal imaging—Intrinsic signal imaging was performed on the STOMPM microscope or on the Thorlabs Bergamo II. The cortex was illuminated with blue light to obtain a blood vessel map, after which collimated 630 nm light from an LED (Thorlabs) was directed onto the surface of the brain to measure intrinsic hemodynamic responses. Visually evoked responses were collected at 50 Hz using an Andor Xyla camera. Visual stimuli were blockwise grating stimuli (8s on, 8s off, 0.06-0.1 cycles per degree, 16 directions).

Analysis—Intrinsic imaging single-condition maps were computed by comparing whether reflectance changes evoked by a single-stimulus condition could be discriminated from reflectance changes evoked across all presented stimuli (Purushothaman and Khaytin, 2009). To discriminate a single-condition stimulus at each pixel, reflectance changes across all stimuli were combined into a normalized histogram, and then a pixel's single condition response was computed non-parametrically as the probability of the area under a ROC curve (using the trapezoidal rule). Maps were filtered using a bandpass fermi filter (Purushothaman and Khaytin, 2009). Measured bouton orientation preferences were compared to the orientation preference of the intrinsic signal orientation preference map contained within the 100 gm two photon field of view. STOMPM stimulation grids were aligned to blood vessel reference maps for intrinsic signal imaging using an affine transform

(MATLAB). We computed binary masks for each stimulation spot, and used these masks to measure intrinsic signal orientation preference at single stimulation spots.

Two-photon imaging data were excluded from analysis if motion along the z-axis was detected. Axon images were corrected for in-plane motion using a piecewise non-rigid motion correction algorithm (Pnevmatikakis and Giovannucci, 2017). ROIs were drawn in ImageJ; dendritic ROIs spanned contiguous dendritic segments and bouton/spine ROIs were circular. Mean pixel values for single ROIs were computed over the imaging time series and imported into MATLAB via MIJ (Sage et al., 2012). ΔF/Fo was computed by defining F0 using a 60s percentile filter (typically 10^{th} percentile), which was then low pass filtered at 0.01 Hz. Bouton responses were computed as the average response to the visual stimulus and were included for analysis if ΔF/Fo exceeded 10%. Boutons used for comparing orientation preferences were required to have at least an OSI > 0.15 and be well-fit ($r^2 > 0.5$) by a double Gaussian equation (Scholl et al., 2013). The double Gaussian equation was used to characterize orientation preference by fitting responses to all grating directions.

For pixel-based analyes of jRGECO1a activity, images were averaged over stimulus repetitions and spatially smoothed (Gaussian, 5 μm). Fluorescence change maps were generated by subtracting the mean image during the blank periods. The hue of each pixel of the orientation maps is set by the preferred angle, the color saturation is proportional to the tuning width and the brightness is proportional to the fluorescence change to the best orientation. Bouton orientation preferences were compared to the orientation preference of the pixel-based map within a 12.5 μm radius of the target bouton.

Membrane potential recordings were median filtered with a 30 to 100 sample window to remove action potentials and binned to 5 ms. Responses to individual stimulus cycles were extracted for V_m and spikes separately. Mean (F_0) and modulation amplitudes (F_1 and F_2) of each cycle were computed via Fast Fourier Transform (Matlab). V_m peak responses were computed as the sum of F_0 and F_1. Orientation tuning and preference of V_m responses was characterized with a double Gaussian equation (Scholl et al., 2013). The double Gaussian equation was used to characterize orientation preference by fitting responses to all grating directions. Orientation selectivity index (OSI) was computed as vector strength of V_m responses (Scholl et al., 2013).

For connectivity mapping, V_m traces were median filtered with a time window of 1.2 ms. We defined the prestimulus V_m as the V_m in the 9 ms before IPSP onset. Because of spontaneous activity *in vivo,* single trials were excluded if cells showed large depolarizations (>5 mV) relative to the prestimulus V_m. Significant IPSPs were defined as average IPSPs exceeding three standard deviations below the mean of the prestimulus V_m. We used the centroid of the significant IPSP field for distance measurements from single cells.

Conductance measurements were made in current-clamp mode (Tan et al., 2011). Multiple current steps depolarized or hyperpolarized the neuron close to the reversal potential for inhibition and excitation, respectively. Leak-subtracted synaptic conductances were computed by estimating G_{leak} using the blank stimulus and then performing a linear fit of measured V_m responses at different current injections. Mean and standard deviation of

synaptic conductances were computed with a bootstrap (100 iterations). Cells were excluded from further analysis if negative conductances were extracted across multiple stimuli.

QUANTIFICATION AND STATISTICAL ANALYSIS

Statistical analyses were preformed in MATLAB. We used two-sided non-parametric Mann-Whitney-Wilcoxon test for paired results, except for the Monte Carlo significance tests which were one-sided. To test whether distributions of bouton orientation preference were significantly different from random, we compared the median difference with a null distribution generated from Monte Carlo simulations (n = 10,000 iterations). For each Monte Carlo simulation, we calculated the median difference between two randomly sampled distributions of orientation preferences drawn from a uniform distribution ranging from 0°to 179°with sample sizes equivalen t to the measured distributions. Correlations were calculated as a Spearman's correlation coefficient unless stated otherwise. Statistical significance was defined as $p < 0.05$. Exact sample sizes and are included in the text or figure legends. Center and dispersion values of data presented are described in the text or figure legends. No estimation of statistical power was performed prior to experiments; animal numbers were minimized to conform to ethical guidelines while accurately measuring parameters of animal physiology.

DATA AND CODE AVAILABILITY

Data and code are available from the corresponding author upon reasonable request.

Supplementary Material

Refer to Web version on PubMed Central for supplementary material.

Acknowledgements

The authors thank David Whitney for help with intrinsic signal imaging and analysis, the Fitzpatrick lab for useful discussions and support, and the GENIE project for access to GCaMP6 and jRGECO1a. We thank the MPFI animal resource center staff for their excellent support. This work was supported grants from the National Institutes of Health (2R01 EY006821-28) and the Max Planck Florida Institute for Neuroscience.

References

Adesnik H, 2017 Synaptic Mechanisms of Feature Coding in the Visual Cortex of Awake Mice. Neuron 95, 1147–1159.e4. doi:10.1016/j.neuron.2017.08.014 [PubMed: 28858618]

Anderson JS, Carandini M, Ferster D, 2000 Orientation tuning of input conductance, excitation, and inhibition in cat primary visual cortex. J Neurophysiol 84, 909–926. doi:10.1152/jn.2000.84.2.909 [PubMed: 10938316]

Baker CA, Elyada YM, Parra A, Bolton MM, 2016 Cellular resolution circuit mapping with temporal-focused excitation of soma-targeted channelrhodopsin. Elife 5. doi:10.7554/eLife.14193

Ben-Yishai R, Bar-Or RL, Sompolinsky H, 1995 Theory of orientation tuning in visual cortex. Proc Natl Acad Sci USA 92, 3844–3848. [PubMed: 7731993]

Bortone DS, Olsen SR, Scanziani M, 2014 Translaminar inhibitory cells recruited by layer 6 corticothalamic neurons suppress visual cortex. Neuron 82, 474–485. doi:10.1016/j.neuron.2014.02.021 [PubMed: 24656931]

Bosking WH, Zhang Y, Schofield B, Fitzpatrick D, 1997 Orientation selectivity and the arrangement of horizontal connections in tree shrew striate cortex. The Journal of neuroscience 17, 2112–2127. [PubMed: 9045738]

Chen T-W, Sun Y, Baohan A, Jayaraman V, Svoboda K, 2013 Ultrasensitive fluorescent proteins for imaging neuronal activity. Nature 499, 295. doi: 10.1038/nature12354 [PubMed: 23868258]

Cossell L, Iacaruso MF, Muir DR, Houlton R, Sader EN, Ko H, Hofer SB, Mrsic-Flogel TD, 2015 Functional organization of excitatory synaptic strength in primary visual cortex. Nature 518, 399–403. doi: 10.1038/nature14182 [PubMed: 25652823]

Dana H, Mohar B, Sun Y, Narayan S, Gordus A, Hasseman JP, Tsegaye G, Holt GT, Hu A, Walpita D, Patel R, Macklin JJ, Bargmann CI, Ahrens MB, Schreiter ER, Jayaraman V, Looger LL, Svoboda K, Kim DS, 2016 Sensitive red protein calcium indicators for imaging neural activity. Elife, 5, e12727. doi: 10.7554/eLife.12727 [PubMed: 27011354]

Dhawale AK, Hagiwara A, Bhalla US, Murthy VN, Albeanu DF, 2010 Non-redundant odor coding by sister mitral cells revealed by light addressable glomeruli in the mouse. Nature neuroscience 13, 1404–1412. doi:10.1038/nn.2673 [PubMed: 20953197]

Dimidschstein J, Chen Q, Tremblay R, Rogers SL, Saldi G-A, Guo L, Xu Q, Liu R, Lu C, Chu J, Grimley JS, Krostag A-R, Kaykas A, Avery MC, Rashid MS, Baek M, Jacob AL, Smith GB, Wilson DE, Kosche G, Kruglikov I, Rusielewicz T, Kotak VC, Mowery TM, Anderson SA, Callaway EM, Dasen JS, Fitzpatrick D, Fossati V, Long MA, Noggle S, Reynolds JH, Sanes DH, Rudy B, Feng G, Fishell G, 2016 A viral strategy for targeting and manipulating interneurons across vertebrate species. Nature neuroscience 19, 1743–1749. doi:10.1038/nn.4430 [PubMed: 27798629]

Douglas RJ, Martin KAC, 2007 Recurrent neuronal circuits in the neocortex. Curr Biol 17, R496–500. doi: 10.1016/j.cub.2007.04.024 [PubMed: 17610826]

Douglas RJ, Martin KAC, 2004 Neuronal circuits of the neocortex. Annu Rev Neurosci 27, 419–451. doi: 10.1146/annurev.neuro.27.070203.144152 [PubMed: 15217339]

Fino E, Yuste R, 2011 Dense inhibitory connectivity in neocortex. Neuron 69, 1188–1203. doi: 10.1016/j.neuron.2011.02.025 [PubMed: 21435562]

Gilbert CD, Wiesel TN, 1989 Columnar specifitiy of intrinsic horizontal and corticocortical connecition in cat visual cortex. Journal of Neuroscience. 9:2432–2442. [PubMed: 2746337]

Heeger D, Heeger DJ, Movshon JA, 1999 Linearity and gain control in V1 simple cells Models of cortical circuits (pp. 401–443). Spring, Boston, MA.

Hirsch JA, Martinez LM, Pillai C, Alonso JM, 2003 Functionally distinct inhibitory neurons at the first stage of visual cortical processing. Nature.

Hofer SB, Ko H, Pichler B, Vogelstein J, Ros H, Zeng H, Lein E, Lesica NA, Mrsic-Flogel TD, 2011 Differential connectivity and response dynamics of excitatory and inhibitory neurons in visual cortex. Nature neuroscience 14, 1045–1052. doi:10.1038/nn.2876 [PubMed: 21765421]

Iacaruso MF, Gasler IT, Hofer SB, 2017 Synaptic organization of visual space in primary visual cortex. Nature 547, 449–452. doi:10.1038/nature23019 [PubMed: 28700575]

Isaacson JS, Scanziani M, 2011 How inhibition shapes cortical activity. Neuron 72, 231–243. doi: 10.1016/j.neuron.2011.09.027 [PubMed: 22017986]

Kätzel D, Zemelman BV, Buetfering C, Wölfel M, Miesenböck G, 2010 The columnar and laminar organization of inhibitory connections to neocortical excitatory cells. Nature neuroscience 14, 100–107. doi: 10.1038/nn.2687 [PubMed: 21076426]

Kuchibhotla KV, Gill JV, Lindsay GW, Papadoyannis ES, Field RE, Sten TAH, Miller KD and Froemke RC, 2017 Parallel processing by cortical inhibition enables context-dependent behavior. Nature neuroscience, 20(1), 62. [PubMed: 27798631]

Lee W-CA, Bonin V, Reed M, Graham BJ, Hood G, Glattfelder K, Reid RC, 2016 Anatomy and function of an excitatory network in the visual cortex. Nature 532, 370–374. doi: 10.1038/nature17192 [PubMed: 27018655]

Levy RB, Reyes AD, 2012 Spatial profile of excitatory and inhibitory synaptic connectivity in mouse primary auditory cortex. The Journal of neuroscience 32, 5609–5619. doi:10.1523/JNEUROSCI.5158-11.2012 [PubMed: 22514322]

Liu B-H, Li Y-T, Ma W-P, Pan C-J, Zhang LI, Tao HW, 2011 Broad inhibition sharpens orientation selectivity by expanding input dynamic range in mouse simple cells. Neuron 71, 542–554. doi: 10.1016/j.neuron.2011.06.017 [PubMed: 21835349]

Martinez LM, Wang Q, Reid RC, Pillai C, Alonso J-M, Sommer FT, Hirsch JA, 2005 Receptive field structure varies with layer in the primary visual cortex. Nature neuroscience 8, 372–379. doi: 10.1038/nn1404 [PubMed: 15711543]

Miller KD, 1994 A model for the development of simple cell receptive fields and the ordered arrangement of orientation columns through activity-dependent competition between ON- and OFF-center inputs. Journal of Neuroscience 14(1), 409–441. [PubMed: 8283248]

Oswald A-MM, Doiron B, Rinzel J, Reyes AD, 2009 Spatial profile and differential recruitment of GABAB modulate oscillatory activity in auditory cortex. The Journal of neuroscience 29, 10321–10334. doi: 10.1523/JNEUROSCI.1703-09.2009 [PubMed: 19692606]

Packer AM, Yuste R, 2011 Dense, unspecific connectivity of neocortical parvalbumin-positive interneurons: a canonical microcircuit for inhibition? The Journal of neuroscience 31, 13260–13271. doi: 10.1523/JNEUROSCI.3131-11.2011 [PubMed: 21917809]

Peirce JW, 2007 PsychoPy--Psychophysics software in Python. Journal of neuroscience methods 162, 8–13. doi :10.1016/j.jneumeth.2006.11.017 [PubMed: 17254636]

Pnevmatikakis EA, Giovannucci A, 2017 NoRMCorre: An online algorithm for piecewise rigid motion correction of calcium imaging data. Journal of neuroscience methods 291, 83–94. doi: 10.1016/j.jneumeth.2017.07.031 [PubMed: 28782629]

Pologruto TA, Sabatini BL, Svoboda K, 2003 ScanImage: flexible software for operating laser scanning microscopes. Biomed Eng Online 2, 13. doi:10.1186/1475-925X-2-13 [PubMed: 12801419]

Priebe N, Mechler F, Carandini M, 2004 The contribution of spike threshold to the dichotomy of cortical simple and complex cells. Nature neuroscience 7(10), 1113. [PubMed: 15338009]

Priebe NJ, Ferster D, 2005 Direction selectivity of excitation and inhibition in simple cells of the cat primary visual cortex. Neuron 45, 133–145. doi:10.1016/j.neuron.2004.12.024 [PubMed: 15629708]

Purushothaman G, Khaytin I, 2009 Quantification of optical images of cortical responses for inferring functional maps. Journal of Neuroscience 101(5), 2708–2724.

Roerig B, Chen B, 2002 Relationships of local inhibitory and excitatory circuits to orientation preference maps in ferret visual cortex. Cereb Cortex 12, 187–198. [PubMed: 11739266]

Rubin DB, Van Hooser SD, Miller KD (2015). The stabilized supralinear network: a unifying circuit motif underlying multi-input integration in sensory cortex. Neuron, 85(2), 402–417. [PubMed: 25611511]

Sage D, Prodanov D, Tinevez J, Schindelin J, Year M, 2012 MIJ: making interoperability between ImageJ and Matlab possible. In ImageJ User & Developer Conference (IUDC'12), pp. 227.

Scholl B, Pattadkal JJ, Dilly GA, Priebe NJ, Zemelman BV, 2015 Local Integration Accounts for Weak Selectivity of Mouse Neocortical Parvalbumin Interneurons. Neuron 87, 424–436. doi: 10.1016/j.neuron.2015.06.030 [PubMed: 26182423]

Scholl B, Tan AY, & Priebe NJ (2013). Strabismus disrupts binocular synaptic integration in primary visual cortex. Journal of Neuroscience, 33(43), 17108–17122. [PubMed: 24155315]

Scholl B, Wilson DE, Fitzpatrick D, 2017 Local Order within Global Disorder: Synaptic Architecture of Visual Space. Neuron 96, 1127–1138.e4. doi:10.1016/j.neuron.2017.10.017 [PubMed: 29103806]

Tan AYY, Brown BD, Scholl B, Mohanty D, Priebe NJ, 2011 Orientation selectivity of synaptic input to neurons in mouse and cat primary visual cortex. Journal of Neuroscience 31, 12339–12350. doi: 10.1523/JNEUROSCI.2039-11.2011 [PubMed: 21865476]

Watkins PV, Kao JPY, Kanold PO, 2014 Spatial pattern of intra-laminar connectivity in supragranular mouse auditory cortex. Front Neural Circuits 8, 15. doi:10.3389/fncir.2014.00015 [PubMed: 24653677]

Wehr M, 2013 Parvalbumin-expressing inhibitory interneurons in auditory cortex are well-tuned for frequency. The Journal of neuroscience 33, 13713–13723. doi:10.1523/JNEUROSCI.0663-13.2013 [PubMed: 23966693]

Wehr M, Zador AM, 2003 Balanced inhibition underlies tuning and sharpens spike timing in auditory cortex. Nature 426, 442–446. doi:10.1038/nature02116 [PubMed: 14647382]

Wertz A, Trenholm S, Yonehara K, Hillier D, Raics Z, Leinweber M, Szalay G, Ghanem A, Keller G, Rozsa B, Conzelmann K-K, Roska B, 2015 PRESYNAPTIC NETWORKS. Single-cell-initiated monosynaptic tracing reveals layer-specific cortical network modules. Science 349, 70–74. doi : 10.1126/science.aab1687 [PubMed: 26138975]

Wilson DE, Scholl B, Fitzpatrick D, 2018 Differential tuning of excitation and inhibition shapes direction selectivity in ferret visual cortex. Nature. doi:10.1038/s41586-018-0354-1

Wilson DE, Smith GB, Jacob AL, Walker T, Dimidschstein J, Fishell G, Fitzpatrick D, 2017 GABAergic Neurons in Ferret Visual Cortex Participate in Functionally Specific Networks. Neuron 93, 1058–1065.e4. doi:10.1016/j.neuron.2017.02.035 [PubMed: 28279352]

Wilson DE, Whitney DE, Scholl B, Fitzpatrick D, 2016 Orientation selectivity and the functional clustering of synaptic inputs in primary visual cortex. Nature neuroscience 19, 1003–1009. doi: 10.1038/nn.4323 [PubMed: 27294510]

Wu C, Ivanova E, Zhang Y, Pan Z-H, 2013 rAAV-mediated subcellular targeting of optogenetic tools in retinal ganglion cells in vivo. PLoS ONE 8, e66332. doi:10.1371/journal.pone.0066332 [PubMed: 23799092]

Wu GK, Arbuckle R, Liu B-H, Tao HW, Zhang LI, 2008 Lateral sharpening of cortical frequency tuning by approximately balanced inhibition. Neuron 58, 132–143. doi:10.1016/j.neuron. 2008.01.035 [PubMed: 18400169]

Yoshimura Y, Callaway EM, 2005 Fine-scale specificity of cortical networks depends on inhibitory cell type and connectivity. Nature neuroscience 8, 1552–1559. doi:10.1038/nn1565 [PubMed: 16222228]

Zhao X, Liu M, & Cang J (2013). Sublinear binocular integration preserves orientation selectivity in mouse visual cortex. Nature communications, 4, 2088.

Highlights

- GABAergic boutons have diverse orientation preferences within orientation domains.
- Single neuron inhibitory input fields originate from diverse orientation domains.
- Conductance measurements show inhibition and excitation are not strictly co-tuned.

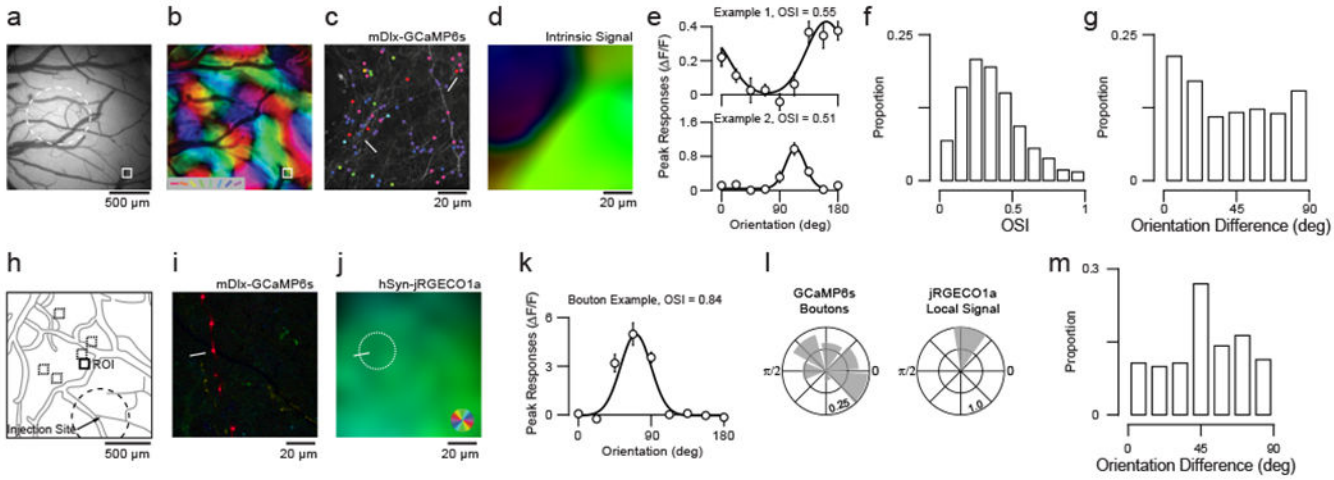

Figure 1. GABAergic axonal boutons exhibit a diverse arrangement of orientation preferences.

(a) Epifluorescence image of injection site (dashed line) with an axon imaging site highlighted (white box). (b) Intrinsic signal polar orientation map for cortical region in (a). (c) Example two-photon projection for site in (a). Visually-responsive and selective (OSI > 0.15) boutons are labeled and pseudocolored based on orientation preferences. (d) Example intrinsic signal polar orientation map for the same two-photon site.

(e) Example orientation tuning of axonal boutons. Data are mean and standard error. Gaussian tuning curves are least-squared fits. (f) Distribution of OSI across all visually-responsive boutons. (g) Distribution of bouton orientation preference difference relative to corresponding local cortical region. (h) Axon imaging sites with respect to the injection site (dashed line). (i) Pixel-based polar orientation map from two-photon imaging of mDlx-GCaMP6s labeled GABAergic boutons (depth = 17 μm) at the ROI indicated in (h). (j) Spatially-smoothed pixel-based polar orientation map for hSyn-jRGECO1a activity (depth = 235 μm) in the same ROI. (k) Example orientation tuning of axonal bouton. Data are mean and standard error. Gaussian tuning curves are least-squared fits. (l) Orientation preference distributions for and corresponding local hSyn-jRGECO1a signal at the ROI indicated in (h). (m) Distribution of orientation preference difference between boutons and local hSyn-jRGECO1a signal. Shown are boutons with OSI > 0.15.

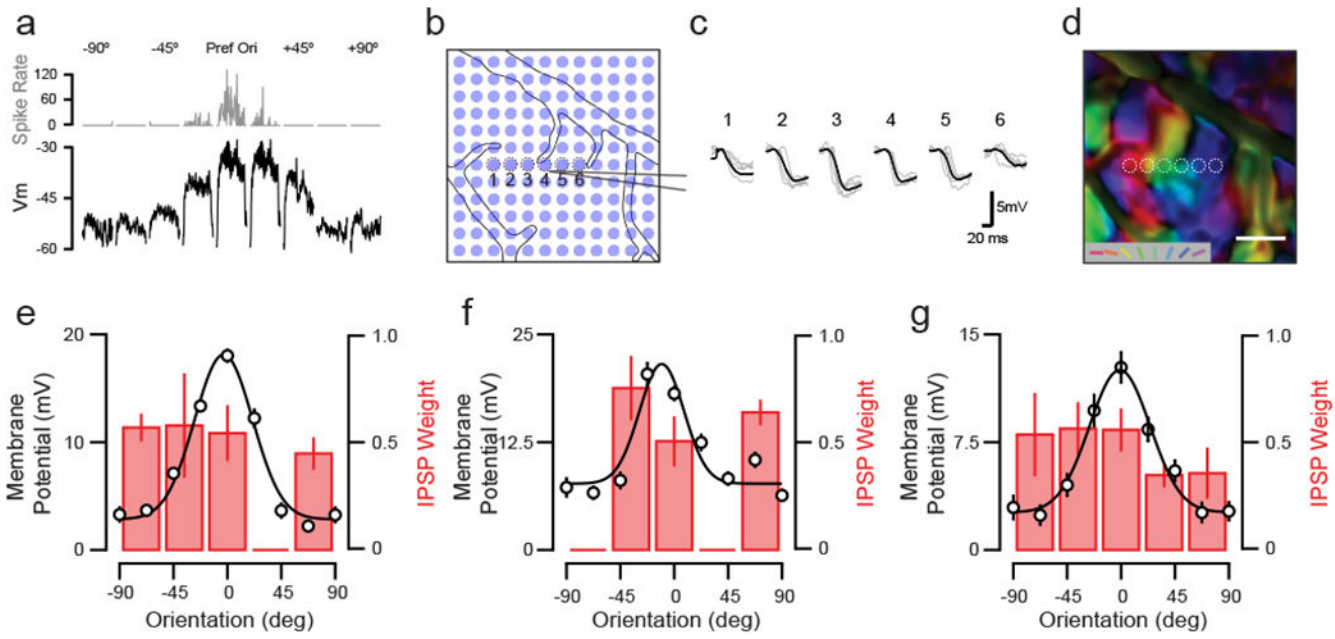

Figure 2. Somatic-targeted optogenetic membrane potential mapping of functional connectivity.

(a) Example whole-cell patch clamp recording of complex cell in layer 2/3 of ferret visual cortex. Shown are spiking (gray, top) and subthreshold V_m (black, bottom) responses to oriented gratings. (b) Image of optogenetic stimulation grid over the cortical surface with visible intracellular pipette. (c) Mean inhibitory postsynaptic potential (IPSP) waveforms evoked by sampled spots in (b) for the cell in (a). (d) Intrinsic orientation preference map for the cortical region overlapping with the IPSP map shown in (c). (e) V_m orientation tuning and IPSP weight for cell in (a). IPSP weight calculated as the average inhibitory input, normalized by IPSP amplitude, relative to spot location in the orientation intrinsic map. Orientation preferences are aligned to the V_m preference. Orientation tuning data points are peak V_m responses. All data shown are mean and standard error. (f-g) Same as in (e) for two example cells and corresponding inhibitory input fields.

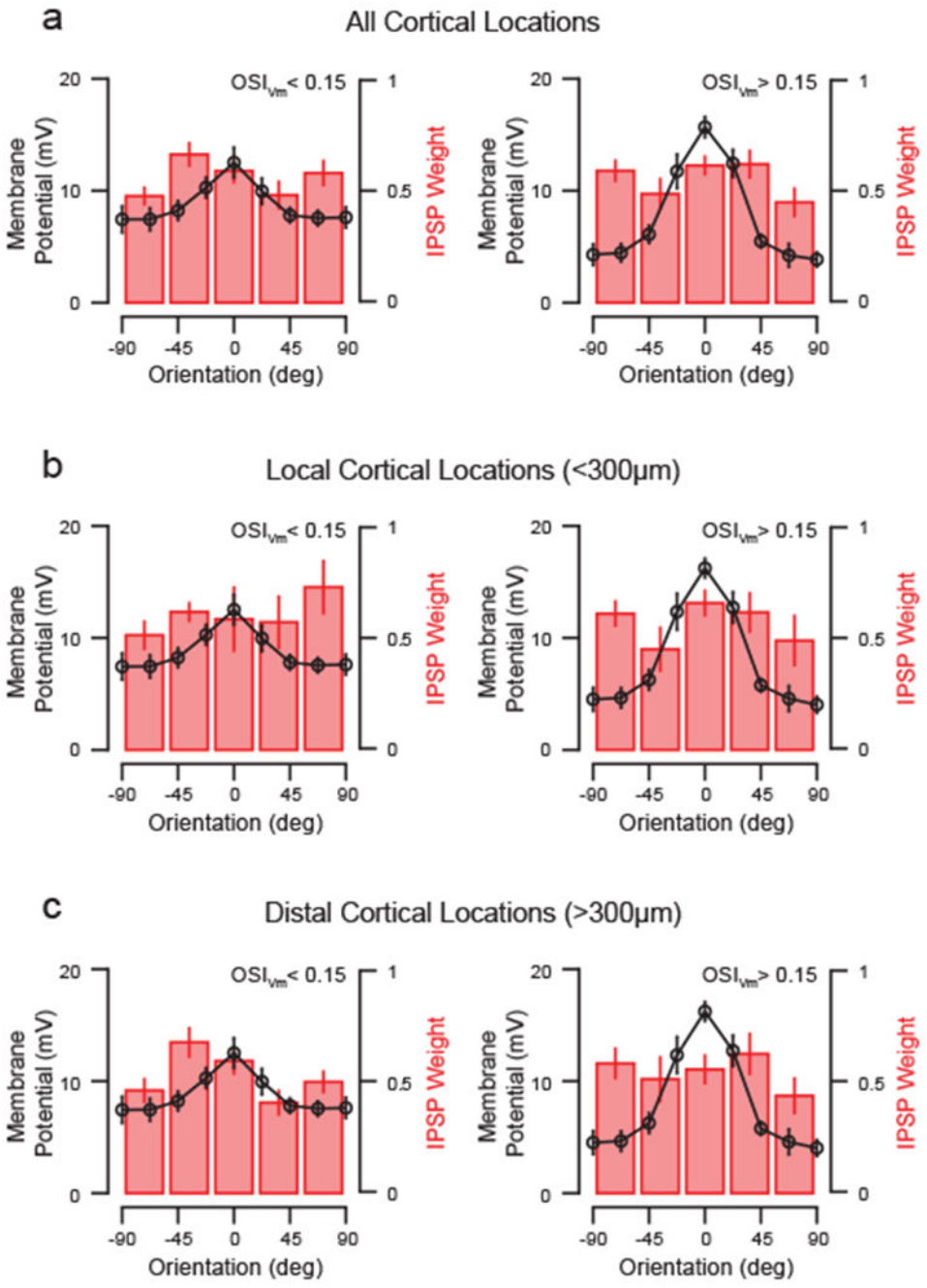

Figure 3. Layer 2/3 inhibitory input fields are broadly tuned for orientation.

(a) Average V_m tuning and IPSP weight for cells with weak orientation selectivity (left) or with moderate to high selectivity (right). Data are mean and standard error. (b) Same as in (a) for stimulated spots less than 300 μm from the recording pipette. (c) Same as in (a) for stimulated spots greater than 300 μm from the recording pipette.

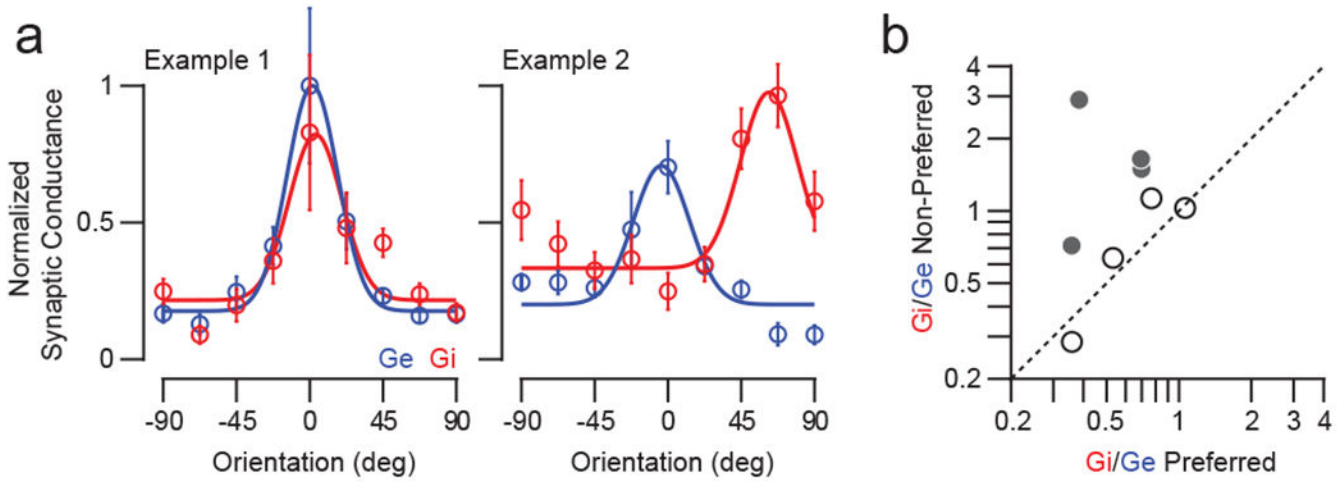

Figure 4. Comparison of inhibitory and excitatory conductance orientation tuning.

(a) Orientation tuning of synaptic conductance from two example cells. Shown are peak responses of inhibition (Gi, red) and excitation (Ge, blue). Data are mean and standard error. Gaussian tuning curves are least-squared fits. (b) Comparison of Gi/Ge for preferred and non-preferred orientations. Filled circles: Cells with significantly different Gi/Ge ratios.

Key Resources Table

Bacterial and Virus Strains		
AAV1.mDlx.GCaMP6s	Dimidschstein et al., 2016	Addgene plasmid # 83899
AAV1.mDlx.ChR2-Flag-Kv2.1.p2a.H2b-CyRFP	Wilson et al., 2018	Addgene plasmids # 89570 and 84356
AAV1/2.hSyn.jRGECO1a	Dana et al., 2016	UPenn Vector Core Cat # AV-1-PV-3849
Biological Samples		
Ferret	Marshall Farms	N/A
Experimental Models: Organisms/Strains		
Ferret	Marshall Farms	N/A
Software and Algorithms		
Cell Magic Wand Tool	This paper	https://github.com/fitzlab/CellMagicWand
StackStitcher	This paper	https://github.com/fitzlab/StackStitcher
MATLAB	Mathworks	https://ch.mathworks.com/products/matlab
FIJI/ImageJ	NIH	http://fiji.sc
Miji	Sage et al., 2012	https://imagej.net/Miji
PsychoPy	Peirce JW, 2007	www.psychopy.org